Microfluid Nanofluid (2007) 3:547–560
DOI 10.1007/s10404-006-0145-0

RESEARCH PAPER

Numerical investigation of AC electrokinetic virus trapping inside high ionic strength media

Jeffery A. Wood · Bingbing Zhang · Matthew R. Tomkins · Aristides Docoslis

Received: 5 September 2006 / Accepted: 30 November 2006 / Published online: 6 January 2007

Abstract A numerical investigation of the mechanism by which viral particles suspended in physiologically relevant (i.e., high ionic strength) media can be electrokinetically sampled on a surface is presented. Specifically, sampling of virus from a droplet is taking place by means of a high frequency non-uniform electric field, generated by energized planar quadrupolar microelectrodes deposited on an oxidized silicon chip. The numerical simulations are based on experimental conditions applied in our previous work with vesicular stomatitis virus. A 3D computer model is used to yield the spatial profiles of electric field intensity, temperature, and fluid velocity inside the droplet, as well as the force balance on the virus. The results suggest that rapid virus sampling can be achieved by the synergistic action of dielectrophoresis and electrothermal fluid flow. Specifically, electrothermal fluid flow can be used to transport the virus from the bulk of a sample to the surface, where dielectrophoretic forces, which become significant only at very small length scales away from the surface, can cause its stable capture.

Keywords AC electrokinetics · Dielectrophoresis · Virus sampling · Surface-based biosensors · Microfluidics

J. A. Wood · B. Zhang · M. R. Tomkins · A. Docoslis (✉)
Department of Chemical Engineering,
Queen's University at Kingston, Dupuis Hall,
Division Street, Kingston, ON, Canada K7L 3N6
e-mail: aris.docoslis@chee.queensu.ca

1 Introduction

Surface-based biosensors are emerging as a set of promising devices with the potential to provide rapid and in-situ detection of biological infectious agents from small sample volumes, potentially without the need for agent amplification (Brake et al. 2003; Hayden et al. 2003; Huang et al. 2001). The operation of these sensors, however, relies on diffusion of the target agents from the bulk of the sample to the capture or detection surface, a rate-limiting process that makes detection of sub-micrometer pathogens (e.g., viruses) from dilute samples (often a requirement for early detection) a great challenge.

Over the last decade, a number of theoretical and experimental studies have demonstrated that this limitation can be overcome with the utilization of AC electrokinetic effects, such as dielectrophoresis, AC electroosmosis, and electrothermal fluid flow. These effects, which are typically generated by energized microelectrode arrays situated onto or in the proximity of the biosensor surface, can cause accelerated transportation and focusing of infectious agents to a surface thus providing detection enhancement while significantly reducing sampling time (Bhatt et al. 2005; Gagnon and Chang 2005; Hughes et al. 1998; Wong et al. 2004). For example, proof-of-principle demonstrations of how dielectrophoresis and AC electroosmosis can be combined into enhancing the detection performance of biosensors have been provided in recent studies (Hoettges et al. 2003; Radke and Alocilja 2005; Wu et al. 2005). Additionally, the overall dimensions of these systems and their ability to effectively concentrate particles from dilute suspensions hold great promise for their integration into microfluidic devices that can

offer rapid sample processing and on-site detection of biological infectious agents.

Dielectrophoresis results from the interaction of the particles with a non-uniform electric field by means of induced polarization effects, directing particles into predetermined locations inside the field. AC electroosmosis originates from the interaction of the tangential component of the electric field with the induced charges in the diffuse double layer on the electrode surface (Morgan and Green 2003). Electrothermal fluid flow is generated by the interaction of the field with the electrically inhomogeneous suspending medium due to local ohmic heating and subsequent development of temperature gradients in the fluid. It has been shown that AC electroosmosis is significant only at lower frequencies (< 100 kHz), whereas at higher frequencies the origin of the fluid flow is predominantly electrothermal (Green et al. 2002).

We have recently demonstrated experimentally that AC electrokinetic phenomena, induced by a planar quadrupolar microelectrode array, can enhance virus sampling from high ionic strength (880 mS m^{-1}, in this case) media and allow the collection and detection of viral particles at low concentrations [10^6 pfu ml^{-1}; (pfu: plaque forming units)] within less than 2 min of sampling time (Docoslis et al. 2004, 2006). The virus studied was vesicular stomatitis virus (VSV), a mammalian, enveloped virus of the *Rhabdoviridae* family with approximate dimensions 173 nm (range 125–205 nm) in length and 75 nm (range 45–85 nm) in diameter (Bradish and Kirkham 1968; Nakai and Howatson 1966). Briefly, the experiments were performed by depositing a small (8 μl) droplet containing the virus on top of a quadrupolar microelectrode array that was fabricated on an oxidized silicon chip (Fig. 1). Prior to each experiment, the microelectrode surface was coated with a (positively charged) layer of poly-L-lysine, in order to (electrostatically) retain the dielectrophoretically captured virus during sample post-processing (immuno-fluorescence assay and imaging). A sinusoidal signal with frequency $f = 1$ MHz and peak-to-peak voltage of 8 V was applied across the four electrodes that were connected to the AC electrical source in an alternating order. The virus in the droplet was exposed to the electric field for a period of 2 min, after which the droplet was removed. Subsequent immunofluorescent staining of the chip surface with a virus-specific antibody revealed significant collection and accumulation of virus in the area between the tips of the four microelectrodes. Dielectrophoretic capture of virus from suspensions of physiologically relevant ionic strength (880 mS m^{-1}) in the concentration range 10^7–10^4 pfu ml^{-1} was attempted and samples of VSV at concentrations as low as 10^6 pfu ml^{-1} were successfully captured and visualized. The experiments generated great promise for the development of biosensors that can provide rapid detection of pathogens from small sample volumes and without the need for concentration amplification prior to analysis. Moreover, it prompted for an investigation of the mechanism causing such virus capture, as well as understanding of the influence of operating parameters, such as exposure time, applied voltage, AC field frequency, electrode configuration, etc. Understanding this mechanism is crucial for the optimization of such biosensor systems.

The present article constitutes a numerical study of the previously described experimental work. A theoretical investigation is carried out with the goal of providing valuable insight into the mechanism by which accelerated virus capture from physiologically relevant media takes place inside non-uniform electric fields created by quadrupolar microelectrode arrays. In addition to dielectrophoresis, electrothermal fluid flow is examined as a factor that can possibly influence the force balance on a virus inside the studied system. An

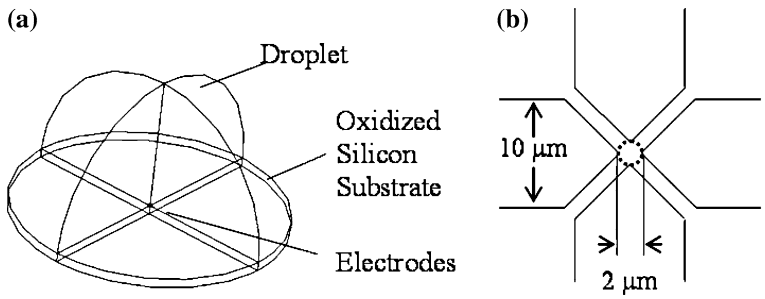

Fig. 1 Schematic representation of the physical model used in the simulations. **a** Sample droplet resting on the oxidized silicon chip containing the quadrupolar microelectrode array; **b** exploded (*top*) view of the centre of the microelectrodes, showing the shape and characteristic dimensions of the electrode tips. The area where accumulation of virus was observed experimentally is outlined by a *circle*

assessment of the intensity of these two phenomena, as well as their relative contribution to the experimentally observed virus capture, is undertaken.

Modelling to explain the effects of AC electric fields on suspended particles inside physiological media and under relatively high frequencies (> 100 kHz) has been used by a number of groups to describe experimentally observed behaviour. A 3D model was presented by Heida et al. (2002) who studied the collection of neuronal cells in a planar quadrupolar microelectrode array with separation between opposite electrodes equal to 100 μm. They showed experimentally that electric field induced fluid flow can transport cells from the suspension to the electrode centre through the interelectrode gap under the influence of fluid flow patterns that conformed with computationally predicted flow caused by buoyancy effects. Since buoyancy effects decay with the third power of the characteristic dimension of the microelectrode system employed, they are expected to be less significant in cases where systems with microelectrode separations smaller by one or two orders of magnitude are used. Sigurdson et al. (2005) used a 2D model to demonstrate the profile of electrothermally generated fluid flow around two parallel electrodes as well as its potential applications to enhance transport of analytes to a surface of a biosensor. Wang et al. (2005) evaluated the fluid flow regime around two ''wedge'' electrodes and assessed the relative contributions of AC electroosmotic and electrothermal effects on the experimentally observed fluid flow using numerical simulations. Recently, Grom et al. (2006) used experiments and modelling to demonstrate how dielectrophoresis and electrothermal fluid flow can be successfully combined towards the trapping of hepatitis A virus in a microelectrode cage (octode electrode array) situated inside a microfluidic chamber. Their modelling results underscored the importance of electrothermal effects by showing that fluid velocities as high as 1.5 mm s^{-1} can be obtained inside media of high ionic strength (300 mS m^{-1}).

The following sections present a numerical approach that is based on a 3D computer model that replicates the conditions of the experiments described earlier (Docoslis et al. 2004, 2006). The voltage, temperature, and fluid flow profiles inside the droplet are solved using the appropriate conservation equations and subsequently used in order to solve the force profile on a viral particle. An explanation of the possible mechanism that causes virus transport and capture in the electrode array is attempted on the basis of the net force (dielectrophoretic and viscous drag force) acting on the particles.

2 Theoretical background

Non-uniform electric fields can influence the motion of particles directly, by means of induced polarization effects (dielectrophoresis), and indirectly, via electrical forces on the suspending medium that result in a fluid flow (electrohydrodynamic effects) and, consequently, a viscous drag force on the particles.

2.1 Direct force on the particle (dielectrophoresis)

When placed inside a spatially non-uniform electric field, a polarizable particle will develop a dipole moment, bringing about a non-zero net force on it due to the action of the non-uniform field on the dipole. The action of this force causes deterministic particle motion, a phenomenon known as dielectrophoresis (DEP) (Pohl 1978). For a spherical particle in cases where moments higher than dipole are ignored, the time averaged value of this force can be calculated from the following equation (Jones 1995):

$$<\vec{F}_{\mathrm{DEP}}> = 2\pi r_{\mathrm{p}}^3 \varepsilon_{\mathrm{M}} \mathrm{Re}[K_e^*] \nabla \left|\vec{E}_{\mathrm{rms}}\right|^2 \quad (1)$$

where, $<\vec{F}_{\mathrm{DEP}}>$ is the time-averaged force, r_{p} is the radius of the polarizable particle, ε_{M} is the real part of the dielectric permittivity of the suspending medium, and $\left|\vec{E}_{\mathrm{rms}}\right|$ is the magnitude of the electric field intensity (root-mean-squared value). The term $\mathrm{Re}[K_e^*]$ is the real part of the effective particle polarizability and is a function of the dielectric permittivities and conductivities of particles and suspending medium, as well as frequency of the applied AC field:

$$K_e^* = \frac{\varepsilon_{\mathrm{p}}^* - \varepsilon_{\mathrm{M}}^*}{\varepsilon_{\mathrm{p}}^* + 2\varepsilon_{\mathrm{M}}^*} \quad (2)$$

From Equation (2) it can be seen that, for a spherical particle, $-0.5 \leq \mathrm{Re}\,[K_e^*] \leq 1.0$. Positive values of the effective polarizability factor give rise to ''positive dielectrophoresis'' (p-DEP), which causes transportation of particles to regions of electric field intensity maxima (typically the electrode edges). The opposite phenomenon ($\mathrm{Re}\,[K_e^*] < 0$) is termed ''negative dielectrophoresis'' (n-DEP) and causes transportation of particles to regions corresponding to electric field intensity minima (e.g., away from the electrodes).

2.2 Indirect forces on the particle (electrohydrodynamic effects)

The applied non-uniform electric field also exerts forces on the suspending medium causing its motion and,

as a result, the development of a viscous drag force on the particles. Two types of electric field-driven fluid flow have been observed: electroosmotic flow and electrothermal flow. AC electroosmosis is generated by the action of the component of the electric field tangential to the electrode plane on the ionic diffuse double layer that develops at the electrode–solution interface and manifests itself as fluid motion in the area over the electrodes. Experimental observations and numerical simulations of AC electroosmotic flow patterns in long planar parallel electrode pairs have shown that the fluid moves in rolls: downwards in the inter-electrode gap and then tangentially outwards over the electrodes (Green et al. 2002). The intensity of this effect can be particularly important at relatively low frequencies (< 100 kHz), but rapidly decays at higher frequencies (Castellanos et al. 2003). Since the present work examines electrohydrodynamic effects at much higher AC frequency (f = 1 MHz) electroosmotic flow is not likely to be present and therefore, it will not be covered in detail later. Dürr et al. (2003) have shown that, in the case of physiological buffers, the threshold frequency above which no significant capacitive effect is expected from the diffuse double layer (i.e., the entire applied voltage is delivered to the interelectrode buffer) is approximately 500 kHz.

The high-intensity electric fields required for the manipulation of sub-micron particles produce significant ohmic heating inside physiological media. Even at relatively low applied voltages, local temperature gradients are likely to develop. These gradients are responsible for spatial variations in the temperature-sensitive electrical properties of the suspending medium, such as conductivity and permittivity, which under the operation of an electric field will bring about a sizeable electrical body force on the medium. The resulting effect is termed electrothermal fluid flow.

The time-averaged electrical body force responsible for the generation of electrothermal fluid flow is given by Morgan and Green (2003):

$$<\vec{f}_e> = \frac{1}{2}\,\mathrm{Re}\left[\frac{\sigma_M\,\varepsilon_M\,(\alpha - \beta)}{\sigma_M + i\,\omega\,\varepsilon_M}\,(\nabla T\cdot\vec{E})\vec{E}^{*} - \frac{1}{2}\,\varepsilon_M\,\alpha\left|\vec{E}\right|^2\nabla T\right] \tag{3}$$

where the parameters $\alpha = (1/\varepsilon_M)(\partial\varepsilon_M/\partial T)$ and $\beta = (1/\sigma_M)(\partial\sigma_M/\partial T)$ capture the effects of temperature gradients on medium permittivity and conductivity, respectively, and * indicates complex conjugate. In the application considered here, there is no spatial variation in the electric field phase, hence $\vec{E}$ can be treated as a real vector and Eq. (3) is simplified to:

$$<\vec{f}_e> = \frac{1}{2}\frac{\varepsilon_M(\alpha-\beta)}{\sigma_M^2 + (\omega\tau_{CR})^2}(\nabla T\cdot\vec{E})\vec{E} - \frac{1}{4}\varepsilon_M\alpha\left|\vec{E}\right|^2\nabla T \tag{4}$$

Where, τ_{CR} is the charge relaxation time of the medium (= ε_M/σ_M). The first term on the right-hand side of Eq. (4) corresponds to the Coulomb and the second to the dielectric component of this force, which act in opposing directions. The Coulomb force dominates below the charge relaxation frequency (approximately equal to 10^9 Hz for a medium with conductivity of 880 mS m^{-1}). It has been observed that, in the case of a field created by two parallel electrode strips, this force causes fluid to move down into the inter-electrode gap and then tangentially out over the electrodes (Morgan and Green 2003). At very high frequencies, the dielectric force will dominate and the flow occurs in the reverse direction to the low frequency case.

The resulting temperature gradients in the electrode vicinity can produce only small buoyancy effects (natural convection) which can be neglected, as indicated by the Grashof number:

$$Gr = \frac{\ell^3\,\rho_M^2\,\beta_T\,g\,\Delta T}{\eta^2} \cong 10^{-6} \tag{5}$$

where, β_T and η are the volumetric thermal expansion coefficient (=210 K^{-1}) and the viscosity of water at room temperature, respectively. The parameter ℓ represents a characteristic dimension of the system and here it has been taken equal to the gap between opposite electrodes (=2 microns).

3 Numerical model

3.1 Calculation of Re[K_e^*]

The effective polarizability factor of the virus, Re [K_e^*], was calculated by approximating the virus as a single-shelled spherical particle of radius $r_{p,eff}$, comprising a dielectrically uniform interior (conductivity σ_{int}, relative permittivity ε_{int}) and a thin, electrically insulating shell with thickness d and surface conductance K_s (Turcu and Lucaciu 1989). A schematic of the model is shown in Fig. 2. Since the actual dielectric parameters for VSV are not known, the present model was formulated so as to represent a general case for a mammalian enveloped virus.

The membrane conductivity, σ_m, is calculated from Arnold and Zimmermann (1988):

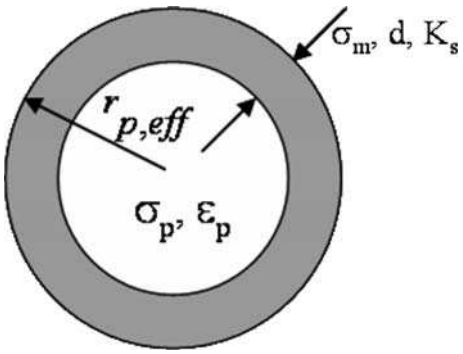

Fig. 2 Schematic representation of a virus particle according to the single-shell model (the parameters are described in the text)

$$\sigma_{\mathrm{m}} = \frac{2\,K_{\mathrm{s}}}{r_{\mathrm{p,eff}}} \tag{6}$$

where, $K_{\mathrm{s}} = K_{\mathrm{s}}^{i} + K_{\mathrm{s}}^{d}$, with K_{s}^{i} and K_{s}^{d} being the conductances of the Stern and diffuse layer, respectively (Hughes 2003). The inclusion of surface conductance effects in the calculations is justified by the fact that the applied AC frequency used in the experiments (1 MHz) is significantly lower than the high-frequency dielectric dispersion limit, i.e., the frequency beyond which double layer effects can no longer influence the particle's dielectrophoretic response. As suggested by O'Brien (1986), for particles with $r_{\mathrm{p}}\kappa > > 1$ (where, r_{p} corresponds to the particle radius and $1/\kappa$ to the Debye length of the double layer surrounding the particle), the high frequency limit of colloidal dielectric dispersion is of the order of κ^2 D (D: diffusivity of ions in the double layer, taken approximately equal to 10^{-9} m^2 s^{-1}), which in the present case (σ_{M} = 880 mS m^{-1}, $1/\kappa \approx$ 1 nm) corresponds to a frequency >100 MHz.

The values of the virus dielectric parameters (Table 1) are assumed to be approximately equal to those reported elsewhere (Hughes et al. 1998). The calculation of membrane conductance was performed according to the method described by Hughes (2003). The values of ionic mobilities were taken as equal to those corresponding to a symmetric electrolyte (KCl).

3.2 Model equations and system geometry

The electric field, temperature, and fluid flow profiles are generated by simultaneously solving the respective balance equations (i.e., conservation of charge, conservation of energy, and conservation of momentum). Each problem is solved in a 3D domain (see Fig. 1a), which replicates the experimental conditions reported in detail elsewhere (Docoslis et al. 2004). The computer model consists of a planar quadrupolar gold microelectrode array, which is deposited on an oxidized silicon substrate. A semi-spherical, 8 μL, drop containing the dilute virus suspension rests over the electrode substrate. The radius of the semi-spherical sample drop is 1.5 mm, the gap between two opposite electrodes is 2 μm, and the total thickness of the oxidized silicon substrate is 100 μm. The equations were solved using the finite element method (FEM) by employing the software package Comsol Multiphysics™ (Burlington, MA, USA). Due to model symmetry, the problems are solved inside one quarter of the model geometry. The boundary equations used in the model are provided in Appendix.

Table 1 Values of the simulation parameters used in the calculation of Re [K_e^*] for a sperical, enveloped virus

$r_{\mathrm{p,eff}}$ (nm)	d (nm)	σ_{int}S/m	$\varepsilon_{\mathrm{int}}/\varepsilon_o$-	ζ-potential (mV)
65	7	0.1	70	–100

3.3 The electrical problem

The time-averaged DEP force is considered only inside electric fields operating at high AC frequencies; therefore the electrical problem can be treated as quasi-electrostatic and solved without employing time-harmonics (e.g., $V = V_o\ \mathrm{e}^{i\omega t}$). According to Gauss's law, the relation of the charge density ρ and electric field strength $\vec{E}_{\mathrm{rms}}$ can be described by:

$$\nabla \cdot (\varepsilon_{\mathrm{M}}\,\vec{E}_{\mathrm{rms}}) = \rho \tag{7}$$

The electric field is given by $\vec{E}_{\mathrm{rms}} = -\nabla V_{\mathrm{rms}}$, where V_{rms} is the electrical potential (root mean-squared value). The charge density was assumed to be zero, resulting in the following final equation:

$$\nabla \cdot (\varepsilon_{\mathrm{M}}\,\nabla V_{\mathrm{rms}}) = 0 \tag{8}$$

3.4 Energy balance

The temperature profile generated due to ohmic heating of the suspending fluid can be calculated from the solution of the energy balance equation (Bird et al. 2002):

$$\rho_{\mathrm{M}}\,C_p\,\frac{\partial T}{\partial t} + \rho_{\mathrm{M}}\,C_p\,\vec{u}\cdot\nabla T = \nabla\cdot(k\nabla T) + \sigma_M\left\langle\left|\vec{E}_{\mathrm{rms}}\right|^2\right\rangle \tag{9}$$

where, ρ_{M} is the mass density, C_p the specific heat at constant pressure, T the temperature, $\vec{u}$ the velocity, k the thermal conductivity, σ_{M} the electrical conductivity

of the medium and $\sigma_M \left|\vec{E}_{rms}\right|^2$ the heat source term. The same equation was also applied to the substrate to account for heat conduction through the silicon chip. The thermal conductivities of silicon dioxide, silicon, and water are taken to be 1.34, 163, and 0.53 J m^{-1} s^{-1} K^{-1}, respectively. The substrate was modelled as one solid domain, using heaviside functions in the z direction to establish the thermal conductivity as that of Si (99 μm) and SiO_2 (1 μm) in the appropriate region of the substrate. An order of magnitude calculation shows that equilibrium is established within a very short time (~10^{-3} s); therefore the temperature profile can be obtained from the solution of Eq. (9) at steady state at this frequency. The final model equation accounts for both conduction and convection at steady-state.

3.5 Momentum balance

The velocity profile inside the medium as a result of the electrothermally induced fluid flow is calculated from the solution of the equation of motion for non-isothermal flow at steady state (Bird et al. 2002):

$$0 = -\rho_M(\vec{u}\cdot\nabla\vec{u}) + \nabla \cdot \left\{-p\vec{I} + \eta\left[\nabla\vec{u} + (\nabla\vec{u})^T\right]\right\} + \rho_M\vec{g} + \vec{f}_e \quad (10)$$

$$\nabla\cdot\vec{u} = 0 \quad (11)$$

where $\vec{f}_e$ is the electrical body force on the fluid, p the local pressure and η the viscosity of the medium. Order of magnitude calculations indicated that the expected variations in temperature (ΔT~13°C) and pressure (Δp~10 Pa) justified the assumption of incompressible fluid. Preliminary simulations employing the Boussinesq approximation showed that buoyancy effects have a negligible impact on the final calculated velocities when compared with the fully incompressible case. Equation (10), however, takes into consideration the effect of viscosity change with temperature, which cannot be neglected for temperature variations of more than a few degrees.

Finally, the viscous drag force on a virus particle (F_{Stokes}) resulting from medium flow is calculated by the Stokes law, which is applicable due to the small particle Reynolds numbers involved:

$$\vec{F}_{Stokes} = 6\pi r_{p,eff}\eta(\vec{u} - \vec{v}) \quad (12)$$

where $\vec{v}$ is the velocity of the virus. In the interest of comparing order of magnitude between F_{DEP} and F_{Stokes}, the particle velocity in the simulations was taken as zero (stationary particles).

3.6 Model assumptions

The calculation of the electric field profile is performed under the assumption that the suspension medium is continuous and dielectrically homogeneous (i.e., there are no spatial variations in the electric charge density). The electrodes were simulated as perfectly conducting (electrically and thermally) materials. Moreover, due to their extremely small thickness (100 nm), they were treated as two-dimensional (flat surfaces). Ohmic heating is considered as the only heat input to the system. Due to the small size of the particles ($r_{p,eff}$ = 65 nm) relative to the characteristic length of the system (2 μm electrode gap spacing), higher order moments in the calculation of the dielectrophoretic force were omitted. Finally, since the concentration of the particles was relatively low and the particles dimensions very small, the field calculations were performed by assuming isolated (non-interacting) particles.

4 Results and discussion

4.1 Dielectrophoretic force

The dielectrophoretic response of the virus is captured by the value of the effective polarizability factor, Re $[K_e^*]$. In Fig. 3, the variation of Re $[K_e^*]$ with respect to the frequency of the applied AC electric field is shown. As can be seen, the virus experiences negative dielectrophoresis over the entire frequency window. This behaviour is typical for many biological particles suspended in physiological buffers and indicates that the medium's effective polarizability is higher than that of the particles. The value of Re $[K_e^*]$ at the conditions of the experiments (1 MHz) is –0.43, close to the

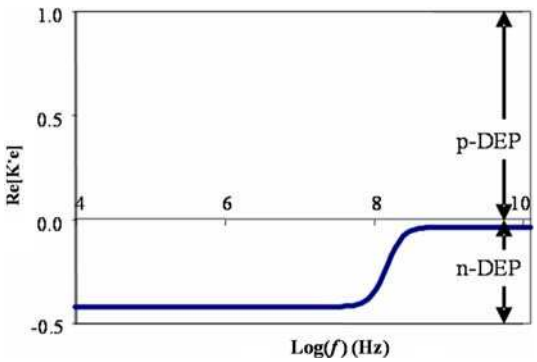

Fig. 3 Plot of the virus effective polarizability factor, Re $[K_e^*]$, as a function of applied AC frequency (f), suggesting that viral particles suspended in a medium with electrical conductivity σ_M = 880 mS/m experience only negative dielectrophoresis

minimum value of –0.5 for a spherical particle. It should also be noted that, although Re $[K_e^*]$ was treated as a function of temperature in the simulations, only small variations (approximately 5%) were observed throughout the simulation domain.

The spatial distribution of the resulting dielectrophoretic force (F_{DEP}) acting on a stationary virus particle was calculated from the solved electric field and temperature profiles. The profile of the force near the electrodes is shown in Fig. 4. The arrows indicate the direction of the F_{DEP} vector (normalized for visualization purposes), whereas the background colors show the logarithmic profile of the magnitude of the force (in N). Figure 4a depicts these variations on a plane normal to the substrate that passes through the tips of opposite electrodes. It can be observed that the force is maximal at the tips of the electrodes. Away from the electrodes the force becomes progressively weaker, forming a local minimum for virus trapping at the centre of the electrode array and immediately above the electrode plane. This location serves as the primary collection area of particles undergoing negative dielectrophoresis. This conclusion is consistent with experimental observations of virus trapping under conditions of negative dielectrophoresis reported elsewhere (Green et al. 1997; Hughes et al. 2001). Outside of this ''dielectrophoretic trap'', the dielectrophoretic force acts to repel the virus away from the electrode tips. Figure 4b captures the variation of F_{DEP} in the interelectrode gap area, corresponding to a plane normal to the electrode substrate that intercepts the electrode edges at right angle as shown in the inset. Local field minima existing midway between adjacent electrodes can also be observed here, predicting a possible secondary virus trap. Figure 4c presents a top view of the force profile on the electrode plane. The force is very strong in the area between the electrodes and decays steeply away from the electrode edges. Viral particles originally situated in the area between the electrode tips are impelled towards the centre of the array (collection area) and those found in the interelectrode gaps are pushed midway between the electrodes. Since the DEP force is repulsive everywhere, it appears that no viral particles can enter through the electrode gaps or approach directly over the electrodes.

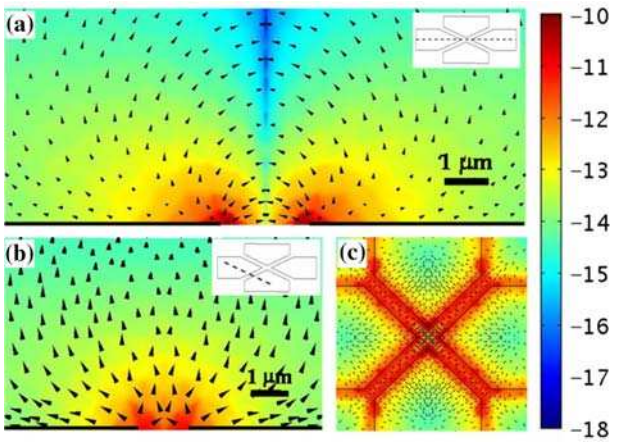

Fig. 4 Spatial profiles of the dielectrophoretic force on the virus. To enhance visual perception, the location of the electrodes is indicated by the *two dark lines* at the bottom of the images. The *insets* indicate where the visualization planes intercept the electrode plane at right angle. **a** Cross-sectional view of the direction of F_{DEP} on a plane passing along the tips of two opposite electrodes. **b** Force profile above the gap between two adjacent electrodes. **c** *Top-down view* of the force profile on the electrode plane. Scale bar in log(N)

If F_{DEP} was the only force acting on the virus then only trapping of particles that originally existed between the electrode tips would be possible. This strongly contradicts experimental observations indicating that the concentration of captured particles increases with time, meaning that another force must also be contributing to particle trapping. This discrepancy is addressed later by considering medium heating effects and the influence of electrothermal flow on the virus.

4.2 Temperature profile

Electrothermal flow in the system is caused by gradients in electric properties, which are induced by gradients in temperature. In the present case, the application of a potential difference of 2.8 V_{rms} across electrodes having a separation $\ell = 2$ microns inside an electrolytic solution of $\sigma_M = 0.88$ Sm^{-1} leads to a local volumetric power dissipation $[W = \sigma_M \times (V_{rms}/\ell)^2]$ of approximately 10^{12} W m^{-3}. As a result of ohmic heating, a significant temperature gradient around the electrodes is developed. Dimensional analysis of the heat balance equation provides an estimate of the resulting temperature rise (ΔT) under the aforementioned conditions. Assuming that heat dissipation in the electrolyte takes place mainly through heat conduction, a maximum value for the expected temperature rise around the microelectrodes can be calculated from Ramos et al. (1998):

$$\Delta T \simeq \frac{\sigma_M V_{rms}^2}{k} \tag{13}$$

According to Eq. (13), the resulting temperature rise varies proportionally with the conductivity of the medium; hence it can become quite significant inside

aqueous media of high ionic strength. Although Eq. (13) predicts a maximum temperature rise of $\Delta T \approx 13°C$, our numerical simulations revealed a smaller temperature rise, as shown in Fig. 5. Figure 5a depicts the temperature profile on the plane that passes through two opposite electrode tips. A maximum temperature of $T = 298.1$ K (25.1°C) can be seen to occur directly at the electrode tips, which corresponds to a temperature rise of 5.1°C above the reference (room) temperature. The difference between FEM simulations and the scaling law is likely based on the substrate only containing a thin insulating layer (1.0 micron of SiO_2) on top of a much larger Si layer, meaning that a great deal of heat will penetrate into the substrate rather than the fluid. As seen in Fig. 5b, however, the developed temperature profile is localized at the microelectrode centre, while the temperature remains uniform in the bulk of the drop and equal to ambient temperature. This sharp decay of temperature with distance from the electrode centre can better be seen in Fig. 5c. In this top-down view of the electrode plane, the temperature is seen to drop to 293 K (room temperature) at a distance of only 15 μm from the centre of the electrodes.

The effect of the applied voltage on the resulting temperature in the medium has been briefly examined. Figure 6 shows the predicted maximum temperature as a function of the potential difference across the electrodes. In all cases, the maximum temperature was observed to occur on the tips of the electrodes. An interesting observation that can be made from Fig. 6 is that the relation between voltage and temperature rise does not follow the exact quadratic relation suggested by Eq. (13), that is, $\Delta T = \sigma_M \times k_M^{-1} \times V^2$. The scaling law overpredicts the temperature rise on average by a factor of 2.5 compared with our simulations, likely due to the fact that the substrate in this case is not a complete insulator but rather a thin layer of silicon dioxide on top of silicon.

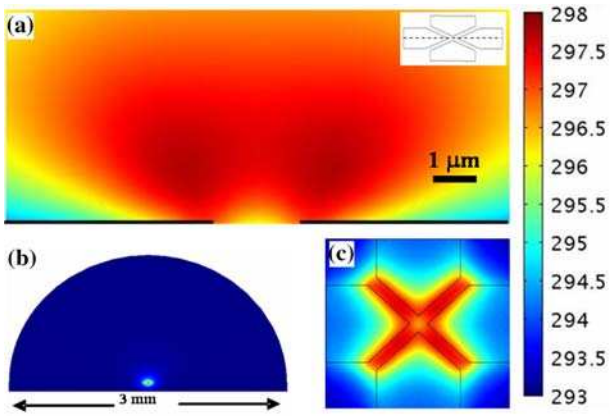

Fig. 5 Temperature profile in the vicinity of the electrodes (at $z = 1$ μm) resulting from ohmic heating in the electrically conducting medium. **a** The maximum temperature rise (5.1 K) is shown to occur at the tips of the electrodes, whereas **b** the bulk of the sample droplet remains at room temperature. **c** Temperature distribution on the electrode plane. Scale bar in Kelvin

4.3 Electrothermal fluid flow effects

As stated earlier, temperature gradients influence temperature-sensitive electrical fluid properties (σ_M, ε_M), causing electrothermal fluid flow. The resulting electrothermal fluid flow patterns are indicated by the arrows in Fig. 7 at three distinct locations around the electrodes. The color bar shows the magnitude of the fluid velocity (in mm s^{-1}). Figure 7a shows the fluid velocity on the plane that passes through the tips of two oppositely situated electrodes. The image shows fluid to move away from the electrodes tips, either tangentially outwards, or from the tips away from the electrode centre, rolling and then coming back down towards the electrode centre. Moreover, a stagnation area can be seen to form at the electrode centre, meaning that fluid flow in this area does not significantly interfere with dielectrophoretic collection of virus. These fluid flow patterns persist throughout the whole drop with decreasing intensity as the distance from the electrodes increases (Fig. 7a, inset). The maximum velocity on this plane can be seen to occur at the tips of the electrodes, reaching values of approximately 6 mm s^{-1}. From this vantage point, fluid appears to approach the centre of the electrode gap from the bulk of the suspension. Figure 7b, which depicts the flow regime in the interelectrode area, presents a flow pattern that is similar with the previous observation. Specifically, fluid is seen to move in circular pat-

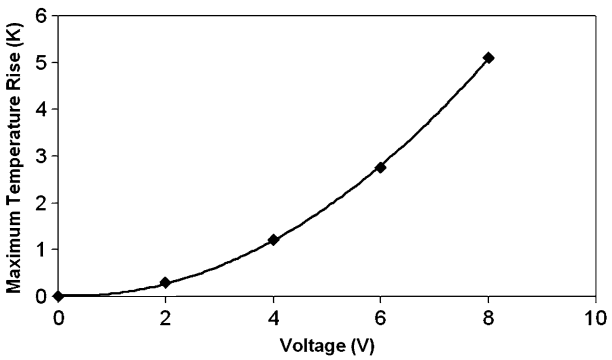

Fig. 6 Plot of the maximum temperature rise observed in the medium as a function of the potential difference applied across the electrodes. The location of the maximum temperatures was at the tips of the electrodes. *Line* represents spline interpolation of simulation data

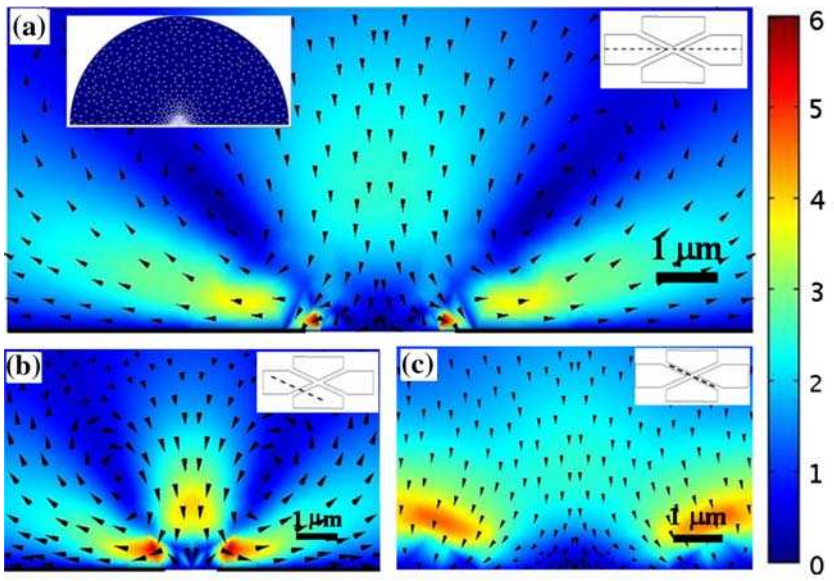

Fig. 7 Electrothermally induced fluid flow patterns generated on the medium due to ohmic heating. The *arrows* (not drawn to scale) indicate the direction of fluid motion. **a** Velocity profile above the tips of opposite electrodes. The *inset to the left* shows the direction of fluid flow inside the whole droplet. **b** Fluid flow patterns in the interelectrode gap where fluid is seen to form rolls. **c** Velocity profile on a plane that runs along the electrode gap. Scale bar in millimeter/second

terns, entering the electrode gaps from above and then escaping tangentially over the electrodes. This type of fluid flow is governed by Coulomb forces on the medium, which drive the fluid from low to high conductivity areas (low to high T, respectively) (Ramos et al. 1998). These strong currents circulate (cold) fluid from the bulk into the electrode centre and also cause fluid rolls above the electrode edges. The highest fluid velocity (~6 mm s^{-1}) is observed right above the electrode gap centre and close to the electrode edges. It can also be seen from the direction of the arrows that the fluid flow does not form a stagnation area between the electrodes, but rather tends to remove particles that can be deposited by the DEP force. Those fluid rolls were also observed experimentally to occur in both parallel electrode pairs (Morgan and Green 2003) and quadrupole electrode arrays (Green et al. 2000). Another interesting observation plane (Fig. 7c) is the one that is normal to the electrode substrate and runs along the centre of the electrode gap between two adjacent electrodes. This plane suggests that there is not a significant fluid flow along this electrode channel towards the electrode centre and thus the rolls that occur normal to the electrode channel may not result in transport of particles to the centre.

Figure 8 presents a panoramic image of the motion that the fluid undergoes in the area immediately above the electrode centre. The four plots shown in the figure represent the magnitude of the velocity component that is normal to the observation plane (z-direction) at various heights above the electrode plane. Positive values of fluid velocity indicate medium flowing upwards. Figure 8a shows the location of the electrode tips, and corresponds to the zero-velocity plane ($z = 0$ μm). In Fig. 8b, the flow profile of a plane at $z = 2$ μm above the electrodes is shown. Fluid is flowing downwards over the interelectrode gap and then escapes tangentially and upwards over the electrode edges along this plane. The maximum velocity in the z-direction occurs in the middle of the long interelectrode gap. The maximum flow rate occurs slightly behind the tips of the electrodes moving fluid upwards. The stagnation zone is visible in the centre, surrounded by the electrode tips. Figure 8c corresponds to a height $z = 3$ μm, where the region that drives fluid downwards becomes wider, suggesting that fluid is moving down as if flowing through a "funnel". Overall, the observed velocities are lower than at $z = 2$ μm, and the loci of maximum velocity have moved slightly away from the electrode tips. Finally, in Fig. 8d ($z = 5$ μm) the intensity of the flow subsides and the downward motion over the interelectrode channel is reduced. Furthermore, the path of the fluid coming downwards seems to widen and spread to include regions above the electrodes. Experimental evidence of similar fluid patterns over quadrupolar electrodes that were observed with the aid of sub-micron latex beads suspended in the fluid at AC frequencies in the MHz range were also made by Müller et al. (1996). The fluid motion was attributed to electrothermal effects and was seen to enhance the dielectrophoretic trapping efficiency.

4.4 Force balance on the particles

The intense fluid streaming observed around the microelectrodes is expected to produce a significant vis-

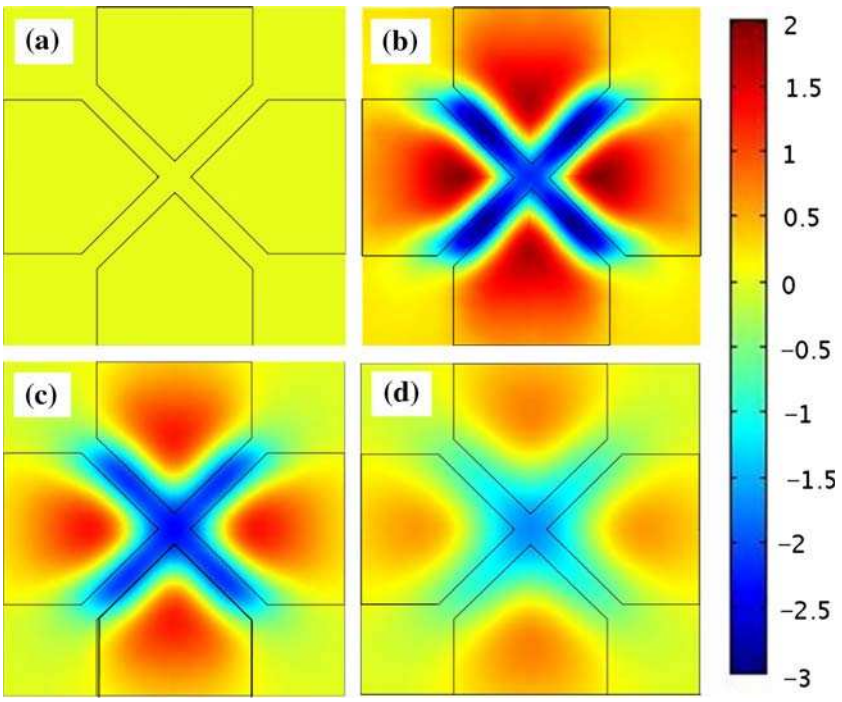

Fig. 8 Spatial variation of the z-component of the fluid velocity in the area immediately above the electrode tips. The *color bar* indicates fluid velocities in millimeter/second. Positive values correspond to fluid moving upwards. Close observation of the color profiles reveals the existence of rolls that circulate fluid into the inter-electrode gaps. **a** $z = 0$ μm; **b** $z = 2$ μm; **c** $z = 3$ μm; **d** $z = 5$ μm

cous drag force on the particle and must be included in the force balance. Moreover, examination of Figs. 4 (F_{DEP} profile) and 7 (velocity profile) indicate that there are many areas where the two forces, namely dielectrophoretic (F_{DEP}) and viscous drag force (F_{Stokes}) tend to cause virus motion in opposite directions. Their relative influence on the resulting virus trajectories becomes immediately apparent, however, when the spatial profile of the net force on the particle is plotted. Figure 9a shows the direction of the combined force vector on the virus as arrows on a surface normal to the microelectrode plane passing through the tips of two opposite electrodes. The colours indicate local values of the magnitude of this force (in N) on a logarithmic scale. Our numerical simulations show that within the stagnation area formed between the electrode tips the magnitude of F_{DEP} is tenfold greater than that of the F_{Stokes}; thus allowing stable particle trapping to occur at the electrode centre. The dielectrophoretic force remains larger only within a radius of approximately 1 μm into the suspension. Beyond this range, the ratio $|F_{\mathrm{Stokes}}| : |F_{\mathrm{DEP}}|$ increases sharply with distance and reaches values 100-fold or higher only a few micrometers away from the electrode centre. Overall, these predictions are in agreement with theoretical estimations provided elsewhere, where the ratio of the virus transport velocities caused by each mechanism varies with distance (x) from the electrodes as follows (Ramos et al. 1998):

$$\frac{u_{\mathrm{Stokes}}}{u_{\mathrm{DEP}}} \propto V^2 \sigma_{\mathrm{M}} \left(\frac{x}{r_{\mathrm{p}}}\right)^2 \tag{14}$$

Due to the balance between the two forces, convective transport of virus particles from the bulk of the medium and into the electrode centre occurs purely by electrothermal fluid flow effects. It is important to note that particle trajectories do not necessarily coincide with this net force as the momentum of particles has been ignored (stationary particles) for simulation purposes. Figure 9b shows that the lack of a strong F_{DEP} above the electrode gap makes the profiles of velocity (Fig. 7b) and net force look identical. Previous experimental studies in our group using fluorescence beads of comparable dimensions ($d = 200$ nm) as tracers confirmed the presence of intense rolls that circulated fluid at high velocities above the electrode gaps at approximately the same positions as those shown in Fig. 9b (Docoslis et al. 2006). Finally, Fig. 9c shows the net force on the particle inside the interelectrode gap. This force profile is shown on a plane of symmetry between two oppositely charged electrodes, so the intensity of the electric field is zero along this plane and hence the force patterns coincide with those shown earlier for the velocity. This figure confirms that the force tends to draw particles from the bulk inwards and towards the electrode centre, although attraction of individual particles towards the trapping locations cannot be inferred with certainty. Experimental

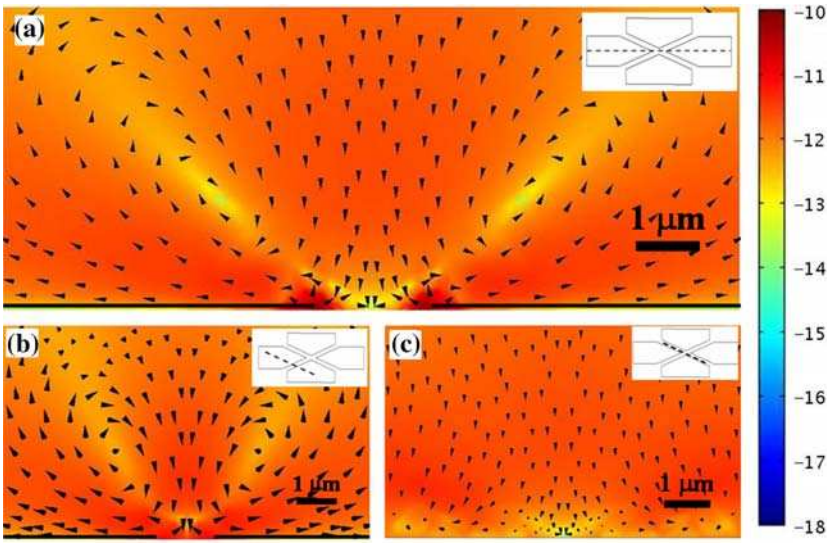

Fig. 9 *Plots* indicating the direction and magnitude of the net force on a stationary virus particle. **a** On a plane that passes from the tips of opposite electrodes, **b** in the electrode gap, and **c** along the interelectrode channel. The dielectrophoretic force appears to be stronger only very close to the electrodes, whereas viscous drag forces dominate outside this range. The synergism between these two effects can cause virus transport from remote areas, as well as stable trapping at the electrode centre

observations reported previously showed that, for the same system, the interelectrode channels served as routes for the transportation of particles to the electrode centre (Docoslis et al. 2006). Specifically, it was observed that the particles transported through the gaps originated from the rolls described earlier. Occasionally, a group of particles from the roll detached and moved towards the electrode centre. A small portion of these particles joined the assembly formed in the electrode centre and the majority moved back into the bulk of the suspension.

The simulation results presented earlier support our conclusion that electrothermal fluid flow plays a major role in the forced transport of particles inside a nonuniform electric field when high ionic strength media are used. The intense fluid flow observed around the electrode centre, however, also suggests that electrothermal flows have the potential to disrupt instead of enhance the virus collection capabilities of DEP under some conditions. An example of how strong the influence of applied voltage can be on the resulting fluid velocities can be seen in Fig. 10, which displays the calculated maximum fluid velocity over the electrodes as a function of the applied voltage. Since the viscous drag (Stokes) force on a stationary particle is given by $\vec{F}_{\text{Stokes}} = 6\pi r_{\text{p}} \eta_{\text{M}} \vec{u}$, a similar voltage effect is expected on the particle motion.

4.5 Experimentally observed particle trapping

Experimental observations using the microelectrodes and experimental conditions described in the simulations section were performed by employing polystyrene beads. The beads used were labelled with the fluorescent dye Suncoast Yellow and had a diameter of 210 nm (Bangs Laboratories Inc., Fishers, IN, USA). 20 μL of the suspension (10^7 particles/mL, 880 mS/m) containing the particles were dispensed directly onto the microelectrodes. Observations of the particle collection patterns on the microelectrodes were conducted with a microscope (Olympus, BX-41) using a 40 × immersion lens (Carl Zeiss, Neoflur). The sample was illuminated by means of a mercury short arc fluorescent lamp (Osram, HBO100W/2) and the images were acquired by a CCD camera (Lumera, Infinity 3). Prior to the onset of an electric field, as shown in Fig. 11a, no fluorescent particles are present in the electrode centre. After applying an electric field of 8 V (peak-to-peak) at a frequency of 1 MHz, the collection of particles was allowed to proceed for approximately 6 min. The experiment resulted in particle collection at the electrode centre as shown in Fig. 11b, with no loss of particles until the field was terminated. The electrodes were constantly monitored to ensure that col-

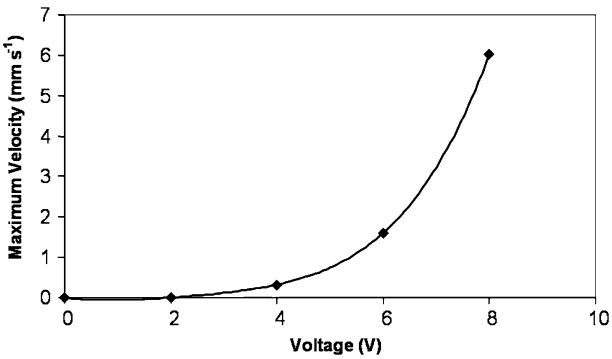

Fig. 10 Plot of the maximum velocity observed over the electrodes as a function of the applied voltage. *Line* represents spline interpolation of simulation data

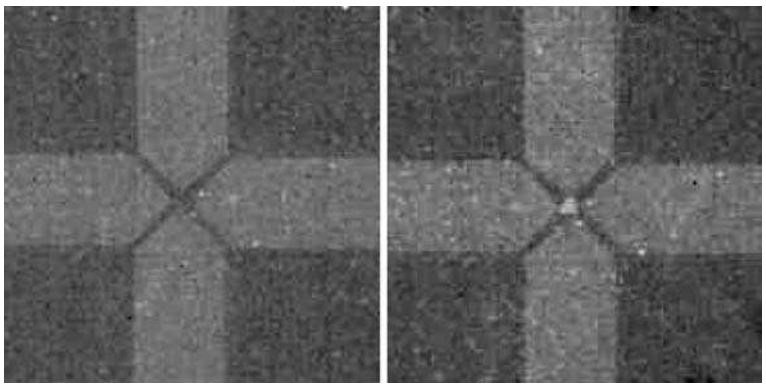

Fig. 11 Experimental evidence of particle trapping using 210 nm fluorescently labelled PS beads. Image (**a**) shows the microelectrodes before the electric field was applied. Image (**b**) shows the collection of fluorescent particles obtained in the microelectrode centre approximately 6 min after the electric field was applied. The microelectrodes and experimental conditions are the same as those considered in the simulations (V_{ptp} = 8 V, f = 1 MHz, σ_M = 880 mS/m, ℓ = 2 μm). Particle concentration: 10^7 particles/mL

lection was not due to the presence of random agglomerates. The observed fluorescent particle collection confirms the ability to collect particles from suspensions having concentrations as low as 10^7 particles/mL and supports the predictions of the simulation that particles become trapped in the electrode centre under the experimental conditions used here.

5 Conclusions

In the present work, 3D numerical simulations are performed in an attempt to explain previously reported experimental results, where non-uniform electric fields were shown to cause accelerated virus transport and capture onto a surface inside media of physiological ionic strength. The results indicate that the virus is transported by electrothermally induced convective currents to the microelectrode vicinity where capture in the centre of the electrode array is accomplished by dielectrophoresis. The induced convective currents are also seen to circulate (cold) fluid from the bulk into the electrode centre and also cause fluid rolls above the electrodes. This fluid motion is so intense that the velocity of the fluid around the electrode centre is found to be on the order of several millimeters per second.

The high electric field intensities needed to manipulate small particles lead to large ohmic heating within a very small volume (mainly the area around the electrode tips) and can give rise to large local temperature increases in the sample. In applications where biological systems are involved, maintaining a well-controlled temperature profile is critical since high temperatures can cause disruption of biological functions (e.g., antibody specificity, enzymatic activity) or biological material damage (e.g., denaturation of viruses), both of which negatively impact sensor performance. The present study, however, shows that microelectrodes embedded into a surface-oxidized silicon wafer (heat conducting material) will result in small temperature rises, mitigating potential adverse effects to biological materials.

Numerical simulations such as those performed here can be valuable tools towards the selection of optimal operating conditions (applied voltage, frequency, electrode design, exposure time) for in situ virus sampling in biosensors, but also assist in the design of point-of-care diagnostic devices and micro-total analysis systems (μTAS) that operate on AC electrokinetic principles.

Acknowledgements The authors would like to acknowledge financial support by NSERC (RGPIN 261691-03) and infrastructure funding by CFI/OIT and Queen's Advisory Research Council. JAW would like to acknowledge the support of NSERC in the form of a PGS D scholarship. MRT would like to acknowledge Queen's University for support in the form of a MacLaughlin scholarship. The fabrication of the microelectrodes was performed at the Cornell Nanofabrication Facility (a member of the National Nanofabrication Users Network), Cornell University, Ithaca, NY, USA.

6 Appendix

6.1 Physical parameters

- The equation for medium density, ρ_M, as a function of temperature T(K) was obtained from data given by Perry et al. (1997):

$$\rho_{\mathrm{M}} = [-3.9854 \times 10^{-6}(T - 273.15)^2 - 3.7765 \times 10^{-5}(T - 273.15) + 1.0001]\rho_0$$

The constant ρ_0 was taken equal to 1,000 kg/m^3.

- Medium conductivity, σ_{M}, was obtained from data regression to experimental measurements on saline water of similar ionic strength (Lide 2001) over the temperature range of interest (T in K):

$$\sigma_{\mathrm{M}} = 0.52 + 0.0171(T - 273.15)$$

- An expression for the relative permittivity of the medium was obtained from data given by Kaatze (1989):

$$\varepsilon_{\mathrm{M}} = 87.297 - 0.3156(T - 273.15)$$

- The viscosity variation of water with temperature T (K) is described by the following equation (Perry et al. 1997):

$$\eta_M = (-0.0077426(T - 273.15)^3 + 1.0344(T - 273.15)^2 - 57.283(T - 273.15) + 1790.8) \times 10^{-6}(\mathrm{kg\,m^{-1}s^{-1}})$$

- Expressions for the parameters α and β were obtained from the derivatives of ε_{M} and σ_{M} (previously shown) with respect to temperature.

$$\alpha = \frac{1}{\sigma_{\mathrm{M}}}\left(\frac{\partial \sigma_{\mathrm{M}}}{\partial T}\right) = \frac{0.0171}{0.471 + 0.0171(T - 273.15)}$$

$$\beta = \frac{1}{\varepsilon_{\mathrm{M}}}\left(\frac{\partial \varepsilon_{\mathrm{M}}}{\partial T}\right) = -\frac{0.3156}{87.297 - 0.3156(T - 273.15)}$$

6.2 Boundary conditions

The following boundary conditions were applied for the solution of the numerical problem:

- Potential difference across opposite electrodes: $\Delta V_{\mathrm{rms}} = 2.8$ V
- External boundaries (medium–air and silicon dioxide–air interfaces):
  - Zero surface charge: $-n{\cdot}D = 0$; (D: electric charge displacement)
  - Isothermal: $T = T_{\mathrm{o}} = 293$°C
  - Slip symmetry: $n \cdot \vec{u} = 0$ (medium–air interface)
- Medium–substrate interface:
  - No-slip condition: $\vec{u} = 0$
- Vertical boundaries (symmetry planes in one quarter of the drop):
  - Surface charge: $-n{\cdot}D = 0$ (symmetry)
  - Heat flux: $-n{\cdot}q = 0$ (symmetry); $q = -k\vec{\nabla}T + \rho_{\mathrm{M}} C_p T \cdot \vec{u}$
  - Slip symmetry: $n \cdot \vec{u} = 0$

References

Arnold WM, Zimmermann U (1988) Electro-rotation: development of a technique for dielectric measurements on individual cells and particles. J Electrostatics 21:151–191

Bhatt KH, Grego S, Velev OD (2005) An AC electrokinetic technique for collection and concentration of particles and cells on patterned electrodes. Langmuir 21:6603–6612

Bird RB, Stewart WE, Lightfoot EN (2002) Transport phenomena, 2nd edn. Wiley, New York

Bradish CJ, Kirkham JB (1968) Morphology of vesicular stomatitis virus (Indiana C) derived from chick embryos or cultures of BHK21/13 cells. J Gen Microbiol 44:359–371

Brake JM, Daschner MK, Luk Y-Y, Abbott NL (2003) Biomolecular interactions at phospholipid-decorated surfaces of thermotropic liquid crystals. Science 302:2094–2097

Castellanos A, Ramos A, González A, Green NG, Morgan H (2003) Electrohydrodynamics and dielectrophoresis in microsystems: scaling laws. J Phys D Appl Phys 36:2584–2597

Docoslis A, Tercero-Espinoza LA, Israel BA, Alexandridis P, Abbott NL (2004) Dielectrophoretic capture of viral particles from media of physiological ionic strength. AIChE Conf Proc 134a

Docoslis A, Tercero Espinoza LA, Zhang B, Cheng L, Israel BA, Alexandridis P, Abbott NL (2006) Using non-uniform electric fields to accelerate the transport of viruses to surfaces from media of physiological ionic strength. Langmuir (in press)

Dürr M, Kentsch J, Müller T, Schnelle T, Stelzle M (2003) Microdevices for manipulation and accumulation of micro- and nanoparticles by dielectrophoresis. Electrophoresis 24:722–731

Gagnon Z, Chang H-C (2005) Aligning fast alternating current electroosmotic flow fields and characteristic frequencies with dielectrophoretic traps to achieve rapid bacteria detection. Electrophoresis 26:3725–3737

Green NG, Morgan H, Milner JJ (1997) Manipulation and trapping of sub-micron bioparticles using dielectrophoresis. J Biochem Biophys Methods 35:89–102

Green NG, Ramos A, Morgan H (2000) AC electrokinetics: a survey of sub-micrometre particle dynamics. J Phys D Appl Phys 33:632–641

Green NG, Ramos A, González A, Morgan H, Castellanos A (2002) Fluid flow induced by nonuniform ac electric fields in electrolytes on microelectrodes. III. Observation of streamlines and numerical simulation. Phys Rev E 66:026305

Grom F, Kentsch J, Müller T, Schnelle T, Stelzle M (2006) Accumulation and trapping of hepatitis A virus particles by electrohydrodynamic flow and dielectrophoresis. Electrophoresis 27:1386–1393

Hayden O, Bindeus R, Haderspock C, Mann K-J, Wirl B, Dickert FL (2003) Mass-sensitive detection of cells, viruses and enzymes with artificial receptors. Sens Actuators B Chem 91:316–319

Heida T, Rutten WLC, Marani E (2002) Understanding dielectrophoretic trapping of neuronal cells: modelling electric field, electrode–liquid interface and fluid flow. J Phys D Appl Phys 35:1592–1602

Hoettges KF, Hughes MP, Cotton A, Hopkins NAE, McDonnell MB (2003) Optimizing particle collection for enhanced surface-based biosensors. IEEE Eng Med Biol Mag 22(6):68–74

Huang L-F, Yang H-H, Su C-C, Wu T-Z, Chen L-K (2001) Application of simultaneous immunosensor for early detection of Dengue virus.Chem Sens 17(Suppl B):478–480

Hughes MP (2003) Nanoelectromechanics in engineering and biology. CRC Press, Boca Raton

Hughes MP, Morgan H, Rixon FJ, Burt JPH, Pethig R (1998) Manipulation of herpes simplex virus type 1 by dielectrophoresis. Biochim Biophys Acta 1425:119–126

Hughes MP, Morgan H, Rixon FJ (2001) Dielectrophoretic manipulation and characterization of herpes simplx virus-1 capsids. Eur Biophys J 30:268–272

Jones TB (1995) Electromechanics of particles. Cambridge University Press, New York

Kaatze U (1989) Complex permittivity of water as a function of frequency and temperature. J Chem Eng Data 34:371–374

Lide DR (2001) Handbook of chemistry and physics, 81st edn. CRC Press, London

Morgan H, Green NG (2003) AC electrokinetics: colloids and nanoparticles. Research Studies Press Ltd., Baldock

Müller T, Gerardino A, Schnelle T, Shirley SG, Bordoni F, De Gasperis G, Leoni R, Fuhr G, (1996) Trapping of micrometre and sub-micrometre particles by high-frequency electric fields and hydrodynamic forces. J Phys D Appl Phys 29:340–349

Nakai T, Howatson AF (1966) The fine structure of vesicular stomatitis virus. Virology 35:268–281

O'Brien RW (1986) The high-frequency dielectric dispersion of a colloid. J Colloid Interface Sci 113:81–93

Perry RH, Green DW, Maloney JO (1997) Perry's Chemical Engineers' Handbook, 7th edn. McGraw-Hill, New York

Pohl HA (1978) Dielectrophoresis. Cambridge University Press, Cambridge

Radke SM, Alocilja EC (2005) A microfabricated biosensor for detecting foodborne bioterrorism agents. IEEE Sens J 4:744–750

Ramos A, Morgan H, Green NG, Castellanos A (1998) AC electrokinetics: a review of forces in microelectrode structures. J Phys D Appl Phys 31:2338–2353

Sigurdson M, Wang D, Meinhart CD (2005) Electrothermal stirring for heterogeneous immunoassays. Lab Chip 5:1366–1373

Turcu I, Lucaciu CM (1989) Dielectrophoresis: a spherical shell model. J Phys A 22:985–993

Wang D, Sigurdson M, Meinhart CD (2005) Experimental analysis of particle and fluid motion in AC electrokinetics. Exp Fluids 38:1–10

Wong PK, Chen C-Y, Wang T-H, Ho C-M (2004) Electrokinetic bioprocessor for concentrating cells and molecules. Anal Chem 76:6908–6914

Wu J, Ben Y, Battigelli D, Chang H-C (2005) Long-range AC electroosmotic trapping and detection of bioparticles. Ind Eng Chem Res 44:2815–2822